

1 **Satellite-detected large CO₂ release in southwestern North America** 2 **during the 2020–2021 drought and associated wildfires**

3 **Hui Chen¹, Wei He^{2,3*}, Jinxiu Liu¹, Ngoc Tu Nguyen⁴, Frédéric Chevallier⁵, Hua**
4 **Yang^{6*}, Yiming Lv¹, Chengcheng Huang¹, Christian Rödenbeck⁷, Scot M. Miller⁸, Fei**
5 **Jiang², Junjie Liu⁹, Matthew S. Johnson¹⁰, Sajeep Philip¹¹, Zhiqiang Liu¹², Ning**
6 **Zeng^{13,14}, Sourish Basu^{14,15}, David F. Baker¹⁶**

7 ¹School of Information Engineering, China University of Geosciences, Beijing 100083,
8 China

9 ²International Institute for Earth System Science, Nanjing University, Nanjing, Jiangsu
10 210023, China

11 ³Zhejiang Carbon Neutral Innovation Institute, Zhejiang University of Technology,
12 Hangzhou, Zhejiang 310014, China

13 ⁴State Key Laboratory of Hydrology-Water Resources and Hydraulic Engineering, College
14 of Hydrology and Water Resources, Hohai University, Nanjing 210024, China

15 ⁵Laboratoire des Sciences du Climat et de L'Environnement, LSCE/IPSL, CEA-CNRS-
16 UVSQ, Université Paris-Saclay, 91191 Gif-sur-Yvette, France

17 ⁶State Key Laboratory of Remote Sensing Science, Beijing Normal University, Beijing
18 100875, China

19 ⁷Max Planck Institute for Biogeochemistry, Jena, Germany

20 ⁸Whiting School of Engineering, Johns Hopkins University, Baltimore, Maryland 21211,
21 USA

22 ⁹Jet Propulsion Laboratory, California Institute of Technology, Pasadena, CA, USA

23 ¹⁰Earth Science Division, NASA Ames Research Center, Moffett Field, CA, USA

24 ¹¹Centre for Atmospheric Sciences, Indian Institute of Technology Delhi, New Delhi, India

25 ¹²CMA Key Open Laboratory of Transforming Climate Resources to Economy, Chongqing
26 Institute of Meteorological Sciences, Chongqing, 401147, China

27 ¹³Laboratory of Numerical Modeling for Atmospheric Sciences & Geophysical Fluid
28 Dynamics, Institute of Atmospheric Physics, Chinese Academy of Sciences, Beijing, China

29 ¹⁴Earth System Science Interdisciplinary Center, College Park, MD, USA

30 ¹⁵NASA Goddard Space Flight Center, Global Modeling and Assimilation Office,
31 Greenbelt, MD, USA

32 ¹⁶Cooperative Institute for Research in the Atmosphere, Colorado State University, Fort
33 Collins, CO, USA

34 * Corresponding author: Wei He (weihe@nju.edu.cn) or Hua Yang (yh_crs@bnu.edu.cn).

35 Abstract

36 Southwestern North America (SWNA) continuously experienced megadroughts and large
37 wildfires in 2020 and 2021. Here, we quantified their impact on the terrestrial carbon
38 budget using net biome production (NBP) estimates from an ensemble of atmospheric
39 inversions assimilating in-situ CO₂ and Carbon Observatory–2 (OCO-2) satellite XCO₂
40 retrievals (OCO-2 v10 MIP Extension), two satellite-based gross primary production (GPP)
41 datasets, and two fire CO₂ emission datasets. We found that the 2020–2021 drought and
42 associated wildfires in SWNA led to a large CO₂ loss, an ensemble mean of 95.07 TgC
43 estimated by the satellite inversions using both nadir and glint XCO₂ retrievals (LNLG)
44 within the OCO-2 v10 MIP, greater than 80% of SWNA’s annual total carbon sink.
45 Moreover, the carbon loss in 2020 was mainly contributed by fire emissions while in 2021
46 mainly contributed by drought impacts on terrestrial carbon uptake. In addition, the satellite
47 inversions indicated the huge carbon loss was mainly contributed by fire emissions from
48 forests and grasslands along with carbon uptake reductions due to drought impacts on
49 grasslands and shrublands. This study provides a process understanding of how some
50 droughts and following wildfires affect the terrestrial carbon budget on a regional scale.

51 **Keywords:** land carbon uptake, CO₂ emission, atmospheric inversion, Carbon
52 Observatory–2, CO₂ column concentration, drought and wildfires

53 1. Introduction

54 Terrestrial ecosystems significantly reduce the rise of CO₂ in the atmosphere and the rate
55 of global warming by offsetting around a quarter of the world's anthropogenic CO₂
56 emissions ([Friedlingstein et al., 2022](#)). There is growing evidence that human-caused global
57 warming will increase extreme weather and climate events ([Houghton, 2014](#)). In extreme
58 drought events, warm and dry atmospheric conditions coinciding with precipitation deficits
59 greatly exacerbate soil moisture (SM) loss ([De Kauwe et al., 2019](#); [Green et al., 2020](#)),
60 lowering the ability of terrestrial ecosystems to store carbon ([Smith et al., 2020](#)) by

manuscript submitted to *Environmental Research Letters*

1
2
3
4 61 affecting photosynthesis, causing an increase in tree mortality, and causing crop failure
5 62 ([Beillouin et al., 2020](#)).

6
7
8 63 Large-scale droughts have affected many areas of the world in recent decades ([Ciais et al.,](#)
9
10 64 [2005](#); [Gatti et al., 2014](#)), including North America ([Luo et al., 2017](#); [Wolf et al., 2016](#); [Zhao](#)
11
12 65 [and Running, 2010](#)). Southwestern North America (SWNA, 30-45° N, 105-125° W) has
13
14 66 experienced one of the worst hot droughts ever documented between the summers of 2020
15
16 67 and 2021 ([Dannenberg et al., 2022](#); [Williams et al., 2022](#)). Droughts are main climate
17
18 68 extremes for regulating interannual variations of terrestrial carbon uptake at regional scales
19
20 69 ([Qiu et al., 2020](#)). With future drought and heat events expected to increase ([Meehl and](#)
21
22 70 [Tebaldi, 2004](#); [Zacharias et al., 2014](#)), understanding the response of terrestrial ecosystems
23
24 71 to drought events is crucial for predicting the fate of terrestrial carbon sinks and future
25
26 72 climate. Recently, several studies have paid attention on the impact of the southwest U.S.
27
28 73 droughts in 2020 and (or) 2021 on terrestrial photosynthesis or gross primary production
29
30 74 ([Dannenberg et al., 2022](#); [Zhang et al., 2023](#); [Li et al., 2023](#); [Feldman et al., 2023](#)), yet none
31
32 75 of them studied the impact of the full 2020–2021 event on the terrestrial net carbon uptake,
33
34 76 which would potentially provide a more completed picture about the response of its
35
36 77 ecosystem carbon sequestration to this event.

37
38 78 Atmospheric CO₂ inversions offer large-scale constrained estimates on the dynamic of
39
40 79 terrestrial net carbon uptake, which could offer more objective impact assessment than
41
42 80 using unconstrained terrestrial biosphere model simulations ([He et al., 2023a](#); [He et al.,](#)
43
44 81 [2023b](#)). In-situ CO₂ measurements or spaceborne column-averaged CO₂ dry air molar
45
46 82 fraction (XCO₂) retrievals provide top-down constraints on the net carbon exchange
47
48 83 between the atmosphere and terrestrial ecosystems from regional to global scales, thus
49
50 84 providing an opportunity to study how large-scale carbon fluxes respond to warm and dry
51
52 85 climate features under arid conditions ([Liu et al., 2017](#); [Sun et al., 2017](#)). With more spatial
53
54 86 and temporal coverage relative to in-situ CO₂ measurements, satellite XCO₂ retrievals show
55
56 87 great potential for quantifying the dynamics of regional carbon fluxes ([Bowman et al.,](#)
57
58 88 [2017](#); [Detmers et al., 2015](#); [Philip et al., 2022](#); [Kwon et al., 2021](#)), despite uncertainties in
59
60 89 absolute net flux estimates ([Feng et al., 2016](#)). In addition, satellite-based observations of

manuscript submitted to *Environmental Research Letters*

90 solar-induced chlorophyll fluorescence (SIF) could provide effective constraint on gross
91 primary production (GPP), allowing for a better understanding of the key carbon cycle
92 processes (Li and Xiao, 2019).

93 In this study, we investigated the impact of the 2020–2021 hot droughts and associated
94 wildfires on the carbon cycle in SWNA using the net biome production (NBP) estimates
95 from atmospheric inversions of in-situ CO₂ and Carbon Observatory 2 (OCO-2) satellite
96 XCO₂ retrievals from the OCO-2 v10 Model Intercomparison Project (MIP) Extension,
97 two GPP datasets derived from remote sensing-based data driven models, and two fire CO₂
98 emission datasets. We aimed to answer the following questions: what are the impacts of
99 the 2020 and 2021 drought and associated wildfires on the regional carbon budgets in
100 SWNA, how do the main driving processes (GPP, respiration, and fire emission) contribute
101 to the carbon budget anomalies, and how about the contributions from different ecosystems?

102 **2. Data and Methods**

103 **2.1. OCO-2 v10 Model Intercomparison Project**

104 The OCO-2 MIP is a collaboration among atmospheric CO₂ modelers to study the impact
105 of assimilating OCO-2 retrieval data into atmospheric inversion models. The OCO-2 v10
106 MIP used NASA's operational bias-corrected OCO-2 L2 Lite XCO₂ product v10r retrievals
107 (Byrne et al., 2023; Kiel et al., 2019; <https://daac.gsfc.nasa.gov>). All models were run
108 following a unified protocol, in which they were required to use a same input of assimilated
109 OCO-2 XCO₂ data, data uncertainties, and anthropogenic emissions (e.g., for v10 the
110 ODIAC 2020 was used), but could independently adopt other prior estimates of surface
111 carbon fluxes (NEE, ocean, and fire emissions) (Crowell et al., 2019; Peiro et al., 2022).
112 The outputs cover the time period 2015–2020. Here we used an extended version of OCO-
113 2 v10, which followed the same protocol as v10 MIP but extended through the year 2021.
114 In the OCO-2 v10 MIP Extension, 8 models are included. The detailed information about
115 these models is shown in Table 1.

manuscript submitted to *Environmental Research Letters*

1
2
3
4 116 The estimated fluxes from this intercomparison project have been thoroughly verified and
5
6 117 analyzed for continental carbon budgets over the globe (Byrne et al., 2023). The MIP has
7
8 118 different inversion experiments assimilating various types of observational constraints, and
9
10 119 here we used results from three experiments, including (a) IS: assimilation of in situ CO₂
11
12 120 measurements from international observing networks; (b) LNLG: assimilation of OCO-2
13
14 121 ACOS v10 terrestrial nadir and terrestrial glint XCO₂ retrievals; (c) LNLGIS: Assimilation
15
16 122 of in situ CO₂ measurements and OCO-2 ACOS v10 terrestrial nadir and terrestrial glint
17
18 123 XCO₂ retrievals.
19
20
21
22
23
24
25
26
27
28
29
30
31
32
33
34
35
36
37
38
39
40
41
42
43
44
45
46
47
48
49
50
51
52
53
54
55
56
57
58
59
60

124
125

Table 1. Configuration of each simulation used in the OCO-2 v10 MIP Extension.

Model	Institution	Transport model	Meteorology	Meteorology resolution (degree)	Prior biosphere flux	Inverse method	References
AMES	NASA Ames	GEOS-Chem	MERRA2	4° × 5°	CASA-GFED4.1s	4D-Var	(Philip et al., 2022; Philip et al., 2019)
Baker	CSU	PCTM	MERRA2	1° × 1.25° prior, 4° × 5° opt	CASA-GFED3	4D-Var	(Baker et al., 2010; Baker et al., 2006)
CAMS	LSCE	LMDz	ERA5	1.9° × 3.75°	ORCHIDEE	Variational	(Chevallier et al., 2005; Chevallier et al., 2019a)
CMS-Flux	NASA JPL	GEOS-Chem	MERRA2	4° × 5°	CARDAMOM	4D-Var	(Liu et al., 2021)
COLA	IAPCAS	GEOS-Chem	MERRA2	4° × 5°	VEGAS	EnKF	(Liu et al., 2022)
GCASv2	Nanjing Univ.	MOZART	GEOS-5	2.5° × 1.875°	BEPS	EnKF	(Jiang et al., 2021; He et al., 2023b)
JHU	JHU	GEOS-Chem	MERRA2	4° × 5°	CASA GFED4.1s	GIM	(Chen et al., 2021a; Chen et al., 2021b; Miller et al., 2020)
TM5-4DVAR	Univ. Maryland	TM5	ERA-Interim	2° × 3°	SiBCASA	4D-Var	(Basu et al., 2018; Basu et al., 2013)

126

1
2
3
4
5
6
7
8
9
10
11
12
13
14
15
16
17
18
19
20
21
22
23
24
25
26
27
28
29
30
31
32
33
34
35
36
37
38
39
40
41
42
43
44
45
46
47

2.2. Common atmospheric CO₂ inversions using in-situ data

For comparison, we included the flux estimates from four common global atmospheric CO₂ inversions using in-situ data, including CAMS, Jena CarboScope, NOAA CarbonTracker (CT), and NISMON-CO₂.

The operational CAMS in-situ inversion assimilates measurements from ground-based CO₂ air samples (Chevallier et al., 2019b). The inversion uses a suite of prior estimates of CO₂ surface fluxes (including a climatology of terrestrial biosphere fluxes simulated by the ORCHIDEE model) and uses the LMDz model to represent atmospheric transport driven by the ERA5 horizontal wind fields. The variational formulation of Bayes' theorem is used in the inversion. The CAMS CO₂ inversion release version v21r1 (hereafter referred to as CAMS-surface; 1979–2021) were used. We used monthly averages of the NBP with a geographical resolution of 1° × 1° for this analysis. The CAMS official product v21r1 is not identical to the CAMS product in the MIP ensemble, which imposed a unique processing of the satellite retrievals, a unique database for air-sample measurements and a unique prior fossil fuel emission database. The CAMS official product also benefits from a dedicated quality assurance and quality control process, while the MIP had its own. The Jena CarboScope inversion (http://www.bgcjena.mpg.de/CarboScope/?ID=s10oc_v2022; (Rödenbeck et al., 2003)) provides gridded a posteriori NBP flux estimates that constrained by in-situ CO₂ measurements. In comparison to CAMS, it differs significantly in many aspects, including the priori information and its error structure, the atmospheric transport model, and the assimilated observations. The CarboScope inversion consistently assimilated a fixed number of stations for each version throughout the entire study period. We utilized the s10oc_v2022 version (abbreviated as Jena_s10oc), which assimilated data from 78 surface stations spanning the period of 2010 to 2021. The spatial resolution of the TM3 transport model used in the CarboScope inversion is 3.75° × 5°, with optimized daily fluxes.

We utilized the most recent NBP estimates from the NOAA CT inversions, which comprise the CT2022 release (Jacobson et al. 2023a) extended by the CT Near-Real Time (CT-NRT) release CT-NRT.v2023-4 (Jacobson et al. 2023b). The fluxes for the ocean and land biosphere were optimized by estimating weekly scaling factors for 156 ecoregions spanning the globe. These scaling factors multiplied prior fluxes from upstream biosphere model simulations, and optimization was conducted via a 600-member ensemble of TM5 transport simulations (Krol et

1
2
3 157 [al., 2005](#)) using a 12-week windowed ensemble Kalman filter. Wildfire and fossil-fuel CO₂
4 158 emissions were predetermined. On the other hand, the CT-NRT system uses prior fluxes obtained
5 159 from a statistical flux anomaly model, which is driven by anomalies of temperature, sunlight, and
6 160 precipitation, along with the climatology of optimized fluxes from CT2022. Moreover, the CT-
7 161 NRT simulations are designed to use fewer and provisional CO₂ measurement data from the near-
8 162 real time CO₂ ObsPack product ([Schuldt et al. 2022](#)). CT was initially introduced by [Peters et al.](#)
9 163 ([2005](#)) and has since undergone continuous improvement. The standard CT (CT2022) provides
10 164 monthly 1°×1° global fluxes over the period 2000–2020, and CT-NRT.v2023-4 provides similar
11 165 fluxes over the years 2021 and 2022. It is extensively documented and evaluated
12 166 at <https://carbontracker.noaa.gov/>.

13 167 The NISMON-CO₂ (v2022.1) inversion optimizes surface CO₂ fluxes in accordance with
14 168 atmospheric observations using the 4D-Var algorithm ([Niwa et al., 2022](#)) and the NICAM-TM
15 169 transport model ([Tomita and Satoh, 2004](#)). In NISMON-CO₂ ver. 2021.1, the fossil fuel emission
16 170 data were from the GCP-GridFED ver. 2021.2 ([Jones et al., 2021](#)), and the land use and biosphere
17 171 fluxes were from the VISIT model ([Ito and Inatomi, 2012](#)). The biomass burning emission data
18 172 were obtained from the Global Fire Emissions Database (GFED) ver. 4.1s ([Van Der Werf et al.,](#)
19 173 [2017](#)), and the air–sea CO₂ exchange data were obtained from the JMA ([Iida et al., 2021](#)). The
20 174 observational data were derived from the ObsPack-NRT and the ObsPack-GLOBALVIEWplus
21 175 ([Masarie et al., 2014](#)). Additionally, other independently provided data, specifically versions
22 176 6.1_2021_03-01 ([Schuldt et al. 2021a](#)) and 6.1.1_2021-05-17 ([Schuldt et al. 2021b](#)) of ObsPack-
23 177 GLOBALVIEWplus and ObsPack-NRT were utilized, respectively. NISMON-CO₂ (v2022.1)
24 178 provides monthly 1°×1° global fluxes spanning the period 1990–2021.

23 179 **2.3. Satellite-based GPP datasets**

25 180 Two satellite data-driven GPP-based models GOSIF GPP ([Li and Xiao, 2019](#)) and FluxSat
26 181 ([Joiner et al., 2018](#)) were used in this study. The first model is the Orbiting Carbon Observatory-2
27 182 (OCO-2) global SIF dataset, or GOSIF, and its biome-specific linear relationships with observed
28 183 GPP. The GOSIF-GPP dataset (Version 2) was estimated using a data-driven model in which
29 184 variables reflecting vegetation conditions, meteorological conditions, and land cover information
30 185 are used as model inputs. A more refined SIF product based on the OCO-2 (GOSIF) derivation
31 186 uses the strong linear relationship between GPP and GOSIF to generate the GOSIF GPP dataset.

1
2
3 187 It has been widely applied to describe the spatial and temporal variability of GPP and the response
4 188 of GPP to climate change on a regional or global scale (Constenla-Villoslada et al., 2022; Zhao et
5 189 al., 2022). To make the analyses more robust, we employed another GPP dataset, FluxSat (Version
6
7 190 2), which is derived through a data-driven approach that relies on FLUXNET measurements and
8
9 191 reflectance in the seven spectral bands of the Moderate Resolution Imaging Spectroradiometer
10
11 192 (MODIS), and is calibrated against FLUXNET measurements (Joiner & Yoshida, 2020). In the
12
13 193 analyses, we used the average of GOSIF GPP and FluxSat GPP due to their high consistence.
14
15

16 194 **2.4. Biomass burning emissions**

17
18
19 195 The monthly biomass burning (BB) emissions data from the GFEDv4 and Fire Energetics
20
21 196 and Emissions Research version 1.0 (FEERv1) (Ichoku and Ellison, 2013) were used. GFEDv4 is
22
23 197 an industry-standard global emissions model that provides 3-hourly, daily, and monthly estimates
24
25 198 of global emissions for 42 species at 0.25° spatial resolution since 1997 (Giglio et al., 2013; Wees
26
27 199 et al., 2022). GFED is based on the Carnegie–Ames–Stanford Approach (CASA) biogeochemical
28
29 200 model, which simulates carbon fluxes through satellite-based observations of vegetation, weather,
30
31 201 burned area, and burn integrity. FEERv1 is based on the fire radiative power (FRP) method and is
32
33 202 obtained at a 0.1° spatial grid resolution. It uses the time integration of FRP remote sensing
34
35 203 measurements, allowing a more direct estimation of biomass burning rates and bypassing some of
36
37 204 the uncertainties in biogeochemical simulations required by the burning zone approach. Here, due
38
39 205 to the possible uncertainty in BB estimates, we combined GFEDv4 and FEERv1 data for the
40
41 206 analyses, which will make our analyses more reliable. We found the two datasets have a high
42
43 207 agreement in SWNA, thus used the average of them in the analyses.

44 208 **2.5. Ancillary data**

45 209 To characterize climate and vegetation growth conditions during the 2020–2021 drought event, an
46
47 210 array of ancillary data was employed. These data include precipitation and air temperature
48
49 211 metrological reanalysis data, standardized precipitation evapotranspiration index (SPEI), satellite
50
51 212 soil moisture (SM) and fraction of absorbed photosynthetically active radiation (FAPAR).

52 213 The precipitation and air temperature data were taken from the fifth generation European
53
54 214 Reanalysis (ERA5), which is produced by the European Centre for Medium-Range Weather
55
56
57
58
59
60

1
2
3 215 Forecasts (ECMWF) (Hersbach et al., 2020). This dataset is provided at a spatial resolution of
4 216 0.25° and a monthly time-step.

7 217 The SPEI data were obtained from the global SPEI database (SPEIbase v2.8), which provides
8 218 long-term information on global drought conditions with a spatial resolution of 0.5° and a monthly
9 219 temporal resolution. It has a multiscale character, providing SPEI time scales between 1 and 48
10 220 months. The time scale of SPEI used in this study was 12 months. The SPEI is designed to take
11 221 into account both precipitation and potential evapotranspiration (PET) in determining drought
12 222 (Vicente-Serrano et al., 2010). Thus, unlike the SPI, the SPEI captures the main impact of
13 223 increased temperatures on water demand. When the SPEI value is less than or equal to -0.5,
14 224 drought is considered to have occurred, and a smaller value indicates a higher drought severity.

21 225 The root-zone SM from the Global Surface Evaporation Amsterdam Method (GLEAM v3.6a)
22 226 (Martens et al., 2016) was used to characterize soil moisture stress or drought. The GLEAM root-
23 227 zone SM (v3.6a) was generated by the satellite surface soil moisture product ESA-CCI SM (v02.5)
24 228 through a data assimilation scheme (Martens et al., 2017). We used the monthly averaged SM at a
25 229 spatial resolution of 0.25° .

30 230 FAPAR is a key parameter for vegetation photosynthesis and primary production estimation
31 231 (Claverie et al., 2016). In this study, Global land surface satellite (GLASS) FAPAR products were
32 232 used. GLASS FAPAR is approximated as one minus PAR transmittance across the canopy, which
33 233 can be calculated from GLASS LAI and other variables (Xiao et al., 2015). The GLASS FAPAR
34 234 from MODIS data is an instantaneous value at 10:30 a.m. local time, which is very close to the
35 235 daily average FAPAR. The spatial resolution of the raw GLASS FAPAR data is 0.05° and the
36 236 temporal resolution is 8-day, and was resampled to the monthly scale in this study.

237 **2.6. Calculation of terrestrial carbon flux components**

46 238 NBP is a net signal generated by different biogeochemical processes such as total primary
47 239 productivity (GPP), heterotrophic respiration (Rh) and fire disturbances. Their relative
48 240 contributions to interannual and long-term carbon cycle variability may differ (Ahlström et al.,
49 241 2015; Zeng et al., 2005). Therefore, more efforts are needed to quantify which components
50 242 contribute most to interannual variability in NBP and to correct for average state changes. In this
51 243 study, NBP is mainly used to study the response of terrestrial ecosystems to extreme drought

244 events. A negative sign of NBP indicates the release of carbon to the atmosphere while a positive
245 sign indicates the uptake of carbon from the atmosphere. The carbon balance of terrestrial
246 ecosystems can be expressed by the following equation:

$$247 \quad \text{NBP} = \text{GPP} - \text{Reco} - \text{BB} = \text{NEP} - \text{BB} \quad (1)$$

248 where NEP represents net ecosystem productivity, *BB* represents disturbances such as wildfire,
249 harvesting, grazing, and land cover change, and Reco is the total ecosystem respiration. We
250 decompose the NBP anomalies during the 2020 and 2021 droughts into their different constituent
251 fluxes.

252 In this study, we used the average *BB* data based on the burning region GFEDv4 and the FRP-
253 based FEERv1 for calculating the *BB* anomaly. Reco is the difference between the average of the
254 two GPP datasets (GOSIF GPP and Fluxsat GPP) and NEP, and the derivation equations for NEP
255 and Reco are as follows.

$$256 \quad \text{NEP} = \text{NBP} + \text{BB} \quad (2)$$

$$257 \quad \text{Reco} = \text{GPP} - \text{NBP} - \text{BB} \quad (3)$$

258 **2.7. Calculation of anomaly**

259 Anomalies of carbon fluxes and meteorological, hydrological and vegetation indicators were
260 calculated as follows:

$$261 \quad X'_i = X_i - \overline{X_{\text{BL}}} \quad (4)$$

262 where X'_i denotes the anomaly of variable X in month i of a year, X_i represents the value of
263 variable X in month i of a year, and $\overline{X_{\text{BL}}}$ denotes the average of the monthly data of variable X
264 during a benchmark period. We used the period 2015–2019 as the baseline for drought detection,
265 since for North America this time period is similar to the long term mean and does not have any
266 large anomalous events (<https://droughtmonitor.unl.edu/NADM/TimeSeries.aspx>).

267 **3. Results and Discussion**

268 **3.1. Climate anomalies in SWNA during the 2020–2021 hot drought**

269 We firstly analyzed the hydroclimate anomalies in SWNA from a historical perspective over the
270 period of 2010–2021, which indicate that the years of 2020 and 2021 are among the driest years
271 (figure 1). The SPEI value in 2020 was the unprecedentedly low in 12 years, and was also among

1
2
3 272 the lowest ones in 2021 (figure 1(a)). Similarly, large negative anomalies for both precipitation
4 273 and SM occurred in the second half of 2020 (figure 1(b)). A clear summer-autumn drought in
5 274 2020 was identified by both SPEI and SM, while a clear spring-summer drought in 2021 was
6 275 identified by SPEI, precipitation and SM (figure 1(b)). The 2020–2021 drought was characterized
7 276 by lower air temperatures in spring while higher in summer and by severe deficits in precipitation
8 277 and SM throughout both years (figure S1). The precipitation in 2020 declined sharply to about 43%
9 278 below the average, which persisted until late 2021 (figure S1(b)). The significant decrease in
10 279 precipitation led to a further scarcity of SM in winter 2020 (figure S1(c) and figure 1(b)), which
11 280 condition continued in late summer 2021. An obvious SM drought extended from early summer
12 281 2020 to late summer 2021, accompanying abnormal high summer temperature (heatwaves), which
13 282 shaped the hot droughts during the 2020–2021 period.

14
15 283 We also analyzed the spatial evolution of the hot drought during the period from summer 2020 to
16 284 summer 2021 (figure S2 and figure 1(c)). Spatially, more than 60% of the region experienced
17 285 positive air temperature anomalies in summer 2020 (JJA), with the largest degree of heatwaves in
18 286 Arizona and New Mexico. In autumn 2020, heatwaves further expanded to California (figure
19 287 S3(a)). In winter 2020, nearly 60% of the areas experienced a decrease of precipitation at 1.5 mm
20 288 per day on average (figure S3(b)), which was consistent with a further exacerbation of the lack of
21 289 SM spatially. Starting from May 2020, the severe meteorological drought resulted in large-scale
22 290 SM deficits, when about 94% of this region experienced negative SM anomalies (figure 1(c)). This
23 291 2020 summer drought further developed in the autumn, reached its peak in the winter of 2020,
24 292 continued into the spring of 2021, and started weakening during the summer of 2021. The
25 293 precipitation played an important role (figure S3(b)), while air temperature also contributed largely
26 294 (figure S3(a)). In summary, most of SWNA experienced an intense and prolonged hydrological
27 295 drought from early summer 2020 until late summer 2021.

28
29
30
31
32
33
34
35
36
37
38
39
40
41
42
43
44
45
46
47
48
49
50
51
52
53
54
55
56
57
58
59
60

Accepted Manuscript

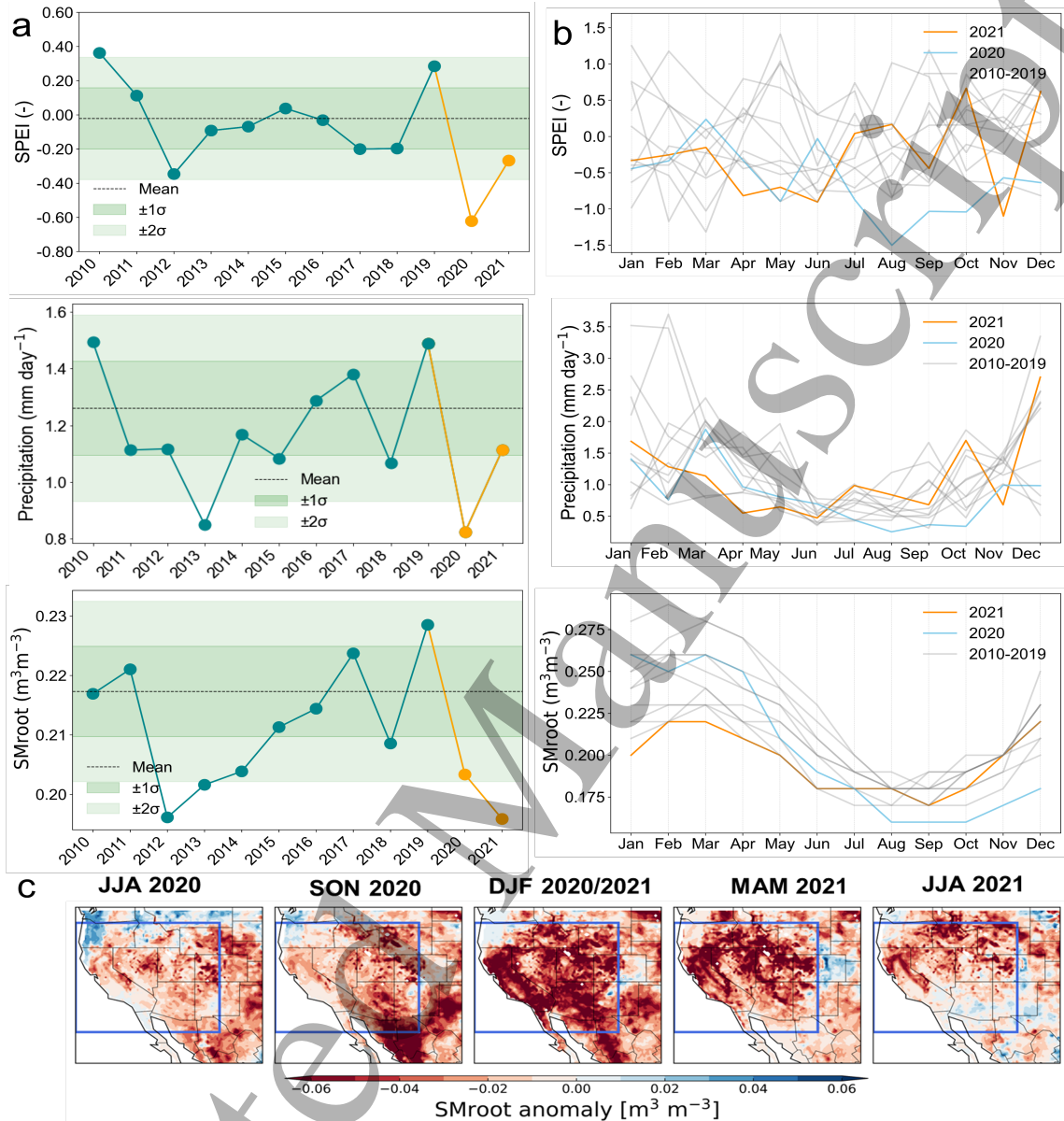


Figure 1. Drought conditions in 2020–2021. (a) Annual mean time series of 12-month scale SPEI, precipitation and root-zone soil moisture (SMroot) from 2010 to 2020; shaded bands indicate one to two standard deviations from the average for the period from 2015 to 2019. (b) Monthly variation of SPEI, precipitation, and SMroot in the SWNA area. The gray lines indicate the years from 2010 to 2019 and the color lines indicate the years of 2020 and 2021. (c) The spatial distributions of the anomalies of SMroot during June–August 2020 (JJA), September–November 2020 (SON), December–February 2020–2021 (DJF), March–May 2021 (MAM), June–August 2021 (JJA). The brown color indicates negative anomalies (decrease), while the blue color indicates positive anomalies (increase).

3.2. Seasonal anomalies in vegetation growth and land carbon uptake

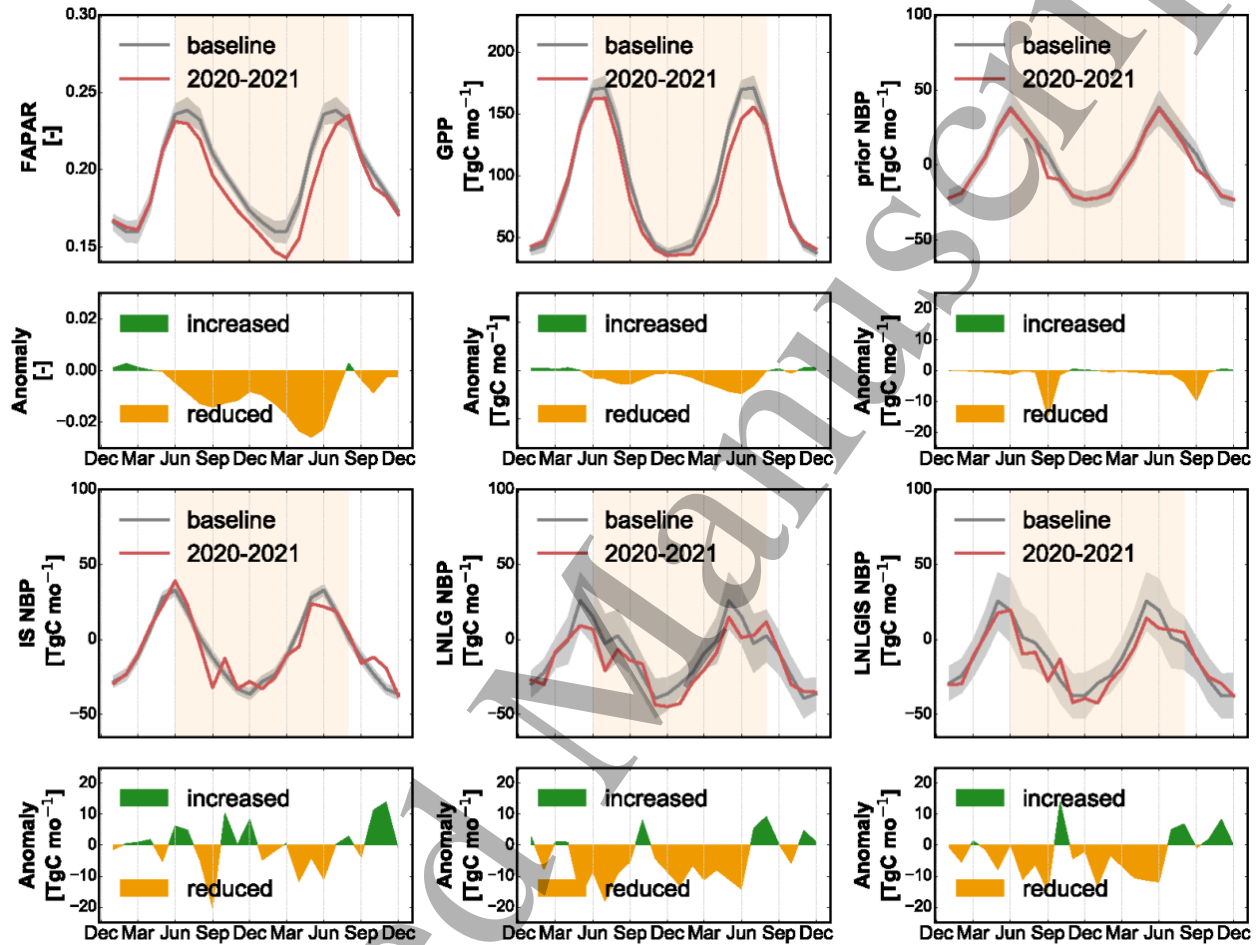
The 2020–2021 drought and wildfires strongly impacted vegetation growth and carbon uptake, causing dramatic reductions in FAPAR and GPP and corresponding seasonal anomalies in NBP

1
2
3 308 (figure 2, tables S1–S4). Over the main drought period (June 2020 – August 2021), FAPAR and
4 309 GPP suffered from continuous declines with the lowest in September 2020 and May – June 2021,
5 310 respectively (figure 2(a) and (b)). Accordingly, there were similar NBP reductions indicated by
6 311 the OCO-2 MIP inversions (figure 2(d–f)), suggesting apparent carbon releases. In the MIP
7 312 inversions, all posterior estimates revealed much stronger NBP anomalies than that shown in the
8 313 prior (figure 2(c)), as well as more consistent timing with the reductions in FAPAR and GPP. Such
9 314 clear NBP reductions in both years were also revealed by the CAMS, Jena CarboScope and
10 315 NISMON inversions; a clear NEP reduction in 2021 was revealed by CarbonTracker while not for
11 316 2020, which could result from the unique feature of CT-NRT by combining a statistical flux
12 317 anomaly model (figure S2). It's worth noting that, all inversion estimates consistently showed a
13 318 rebound in NBP after the main drought period, which may be associated with the enhancement of
14 319 NEP (figure S3) induced by an improved condition in SM availability (figure S1(c)).

20 320 Spatially, the SWNA region experienced a substantial decline in FAPAR during the drought, with
21 321 the most severe decrease in the west, and most of the region experienced suppressed vegetation
22 322 activity in summer (figure S4(a)). A similar decline was observed for GPP, which decreased by
23 323 63% in the spring, with the most severe decrease in northwestern SWNA, followed by the
24 324 northeastern part (figure S4(b)). We analyzed the spatial distribution of seasonal anomalies of NBP
25 325 during the same period (figure S5). The ensemble NBP anomalies for OCO-2 v10 MIP prior were
26 326 nearly neutral (figure S5) while these in the IS, LNLG, and LNLGIS experiments were apparent
27 327 negative, suggesting that the in-situ and satellite-observed atmospheric CO₂ concentrations
28 328 provided effective constraints on NBP anomalies induced by the drought and wildfire event.
29 329 Specifically, the overall NBP anomalies constrained by in-situ CO₂ observations (IS experiment)
30 330 show limited carbon uptake reductions, slightly stronger in the northern part of the SWNA,
31 331 especially in 2020 SON and 2021 JJA (figure S5). The LNLG and LNLGIS NBP anomalies have
32 332 roughly similar spatial patterns and show much stronger carbon uptake reductions in the
33 333 southwestern part of the SWNA in 2020/2021 DJF. More specifically, the longitudinal variation
34 334 in NBP anomalies suggests that the overall NBP anomalies for LNLG and LNLGIS are
35 335 significantly more robust in carbon uptake reductions despite showing considerable inter-model
36 336 discrepancies.

37 337 Overall, the changes in NBP estimated by the OCO-2 MIP inversions generally agree with these
38 338 changes in GPP and FAPAR. They all capture the drought impacts on the terrestrial carbon uptake

339 over SWNA. Their estimated NBP drops abruptly in September 2020 (figure 2(d-f)), when a severe
 340 wildfire event occurred (figures S7 & S8). During summer 2021, there was also a large CO₂ release
 341 due to wildfires.



342
 343 **Figure 2.** Seasonal variations and anomalies in FAPAR, GPP, and NBP over SWNA during 2020–2021 relative to the period of 2015–2019. The NBP estimates were from the prior and posteriors (IS, LNLG and LNLGIS) of
 344 the inversions within the OCO-2 v10 MIP Extension project. The shadowed orange areas indicate the core time period for drought onset.
 345
 346

347 3.3. Event-induced changes of the regional annual carbon budget

348 The total carbon budget anomalies in the SWNA region during 2020–2021 were analyzed. Firstly,
 349 we investigated the main drought period from June 2020 to August 2021 (figure 3(a)). During this
 350 period, the regional NBP experienced a reduction revealed by the in-situ inversions (IS), the
 351 satellite inversions (LNLG) and the inversions constrained with both observations (LNLGIS) from
 352 the OCO-2 v10 MIP Extension project. The prior also estimated a reduction of -25.1 ± 18.9 TgC,
 353 which is comparable with the estimate of -24.5 ± 55.5 TgC in the IS inversion. Although the prior

1
2
3 354 estimated a comparable size of NBP decline, its multi-year average NBP in this region indicated a
4
5 355 carbon source, contrasting with that all the inversions pointed to a carbon sink. With the constraint
6
7 356 of OCO-2 XCO₂ retrievals, the inverse estimates exhibited much larger absolute NBP anomalies
8
9 357 (-95.0 ± 60.6 TgC by LNLG and -69.2 ± 69.9 TgC by LNLGIS) than the IS estimate. Despite large
10
11 358 difference between absolute values of NBP anomalies, both the IS inversion and the satellite
12
13 359 inversion (LNLG) estimated an annual carbon uptake loss greater than 80% (table 2). A
14
15 360 comparable magnitude of NBP reduction was also indicated by the both surface inversions of
16
17 361 CAMS and Jena, albeit that their multi-year average NBPs in this region indicated near carbon
18
19 362 neutral (table 2). Also, the NISMON and CarbonTracker inversions indicated a decrease in NBP,
20
21 363 while their multi-year average NBPs exhibited a contrasting direction in carbon sink or source.
22
23 364 The continuous NBP decline was also found in a number of flux tower observations from the
24
25 365 AmeriFlux network in the SWNA region (figure S8, 18 sites covering the study period), for
26
27 366 example, at sites US-Ses (OSH), US-Seg (OSH), and US-Mpj (WSA). The NBP reduction during
28
29 367 this event was primarily resulting from BB emission, which was as large as 96.8 TgC (figure 3(a)).
30
31 368 Meanwhile, it was partly offset by the increase in NEP, which was slight in the satellite inversion
32
33 369 but much larger on the surface inversion within the MIP, and was also indicated by the CAMS
34
35 370 surface, Jena CarboScope, and NIMSON inversions (Figure 3d). Combining the NBP estimates
36
37 371 from different inversion models with the component flux estimates from a same set of data sources,
38
39 372 the analyses consistently suggested that the increase in NEP resulted from a more considerable
40
41 373 decrease in Reco (-230.41 to -160.52 TgC) than in GPP (-158.8 TgC). The larger inhibition in
42
43 374 Reco than in GPP can also be observed at flux tower observations (figure S8), for example, at sites
44
45 375 US-Var (GRA), US-Wjs (SAV), and US-Bi2 (CRO), where a greater suppression in respiration
46
47 376 during some of the drought and wildfire period leading to an unexpected increase in NEP. Such
48
49 377 unexpected phenomenon is discussed later.

50
51 378 Then, we assessed the anomalies in the regional carbon budgets for the full years of 2020 (figure
52
53 379 3(b) and figure 3(e)) and 2021 (Figure 3(c) and figure 3(f)). The primary mechanisms underlying
54
55 380 the regional carbon balance change of the two years differed markedly. In 2020, fire emissions
56
57 381 (also known as biomass burning, BB) released 68.73 TgC, but NEP increased by 34.25 TgC due
58
59 382 to the compensation of a decline in GPP and a larger attenuation in Reco, leading to a NBP
60
383 decrease by 30.16 TgC on average. In this year, the underlying processes of NEP (GPP and Reco)
384 showed generally smaller reductions than the magnitude of fire emissions, indicating that fires

dominated the carbon budget dynamics in this region. In 2021, the OCO-2 inversions consistently showed a smaller anomaly in NBP and NEP compared to 2020 while much larger reductions in both GPP and Reco. Relative to 2020, the fire emissions were apparently smaller (figure S6(c)). Thus, in 2021, the anomaly of the ecosystem carbon uptake was likely more dominant when compared to the contribution by fire emissions. Surprisingly, NEP increased in both 2020 and 2021 as Reco decreased more than GPP. In particular, Reco was substantially attenuated in 2021, allowing the increased NEP to largely compensate for the carbon losses due to wildfires. In both 2020 and 2021, GPP and Reco were greatly damped, and this attenuation was significantly larger in Reco than in GPP. These flux anomalies were also indicated by most surface inversions of CAMS, Jena, NIMSON and CarbonTracker (figure 3(e-f)).

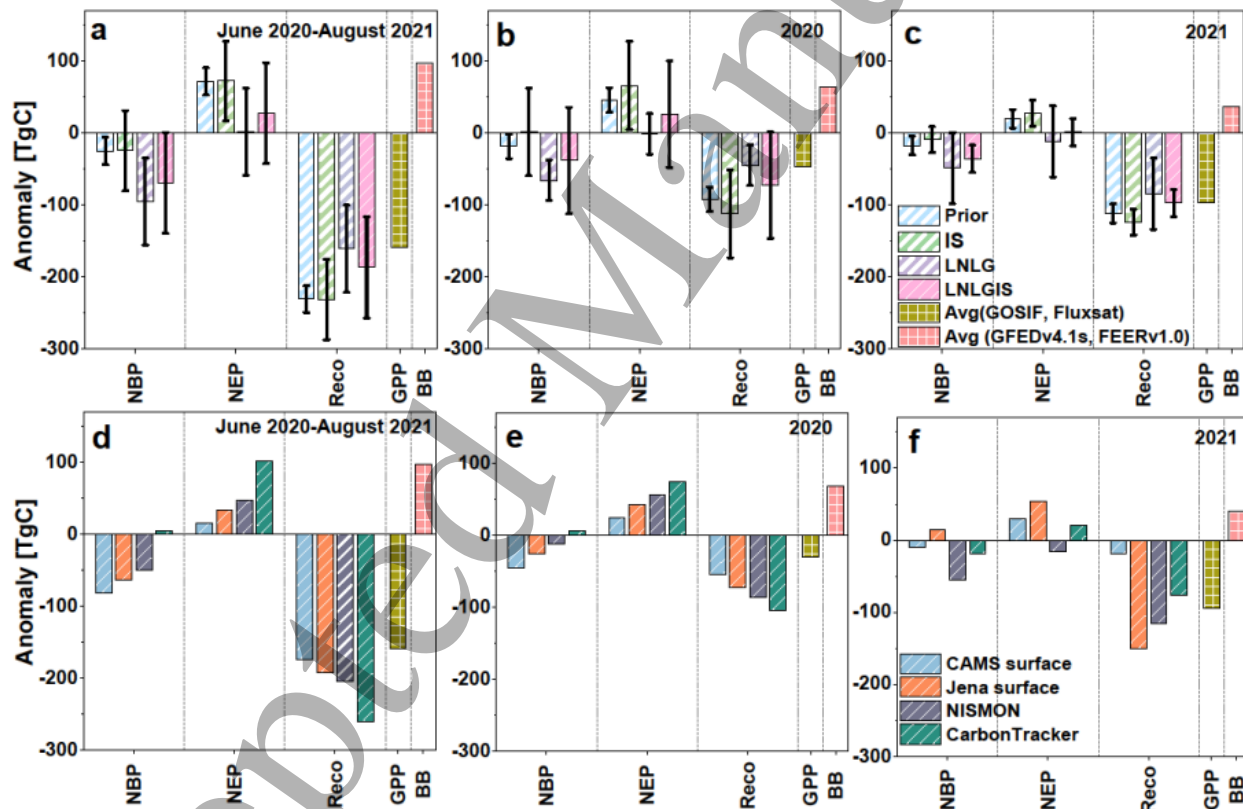


Figure 3. Anomalies of NBP and relevant fluxes in SWNA during 2020–2021. (a-c) OCO-2 MIP results, including PRIOR, IS, LNLG, and LNLGIS, where the error bar indicates a standard deviation; (d-f) CAMS surface, Jena CarboScope, NIMSON, and CarbonTracker inversions. BB indicates the biomass burning emission, which is an average of the GFEDv4 and FEERv1 estimates (the two have almost identical BB values). GPP is an average of the GOSIF and FluxSat GPP estimates (the two have almost identical GPP values).

404 **Table 2.** Regional NBP anomalies during the 2020–2021 drought and wildfire event.

Datasets	Baseline (TgC)	Absolute anomaly (TgC)	Relative change
OCO-2MIP Prior	102.84 ± 25.8	-25.18 ± 18.9	-24%
OCO-2 MIP IS	-28.40 ± 57.6	-24.57 ± 55.5	-87%
OCO-2 MIP LNLG	-114.11 ± 50.3	-95.07 ± 60.6	-83%
OCO-2 MIP LNLGIS	-114.58 ± 55.29	-69.21 ± 69.9	-60%
CAMS surface v21r1	0.11	-81.63	/
Jena surface s10oc_v2022	-0.05	-63.88	/
NISMON-CO2_v2022.1	-43.89	-50.33	-115%
CarbonTracker 2022	71.6	-4.55	-6%

405
 406 To better understand the changes in purposes regional carbon budgets from the ecosystem level,
 407 we investigated the contribution of different ecosystems to the carbon balance anomalies (figure
 408 4). The four dominant ecosystems were forests (4.06%), shrubs (17.14%), grasslands (49.61%),
 409 and crops (2.68%), with the spatial distributions shown in figure S9. Here we made statistics on
 410 the LNLG inversion result. As an arid area, most of the SWNA are covered by grass and shrubs,
 411 which are drought-vulnerable vegetation and usually contribute sizeable flux emission during
 412 droughts. Among them, drought and wildfires had a huge impact on the NBP of grasslands and
 413 shrublands, with grasslands contributing almost half of the total while forests contributed a much
 414 less proportion (only 8%, see figure 4e). In terms of BB contribution, forests and grasslands
 415 contributed about 44% and 52% of carbon loss, respectively. In comparison, the BB emissions by
 416 the shrubland ecosystem and the crop ecosystem were much smaller, for which the decline in NBP
 417 was mainly driven by the ecosystem carbon uptake, i.e., NEP. The OCO-2 MIP inversions broadly
 418 showed that the event caused significant suppressions in both GPP and respiration, leading to a
 419 decrease in NEP, i.e., drought caused a decrease of NBP for the shrubland and crop ecosystems.

Accepted Manuscript

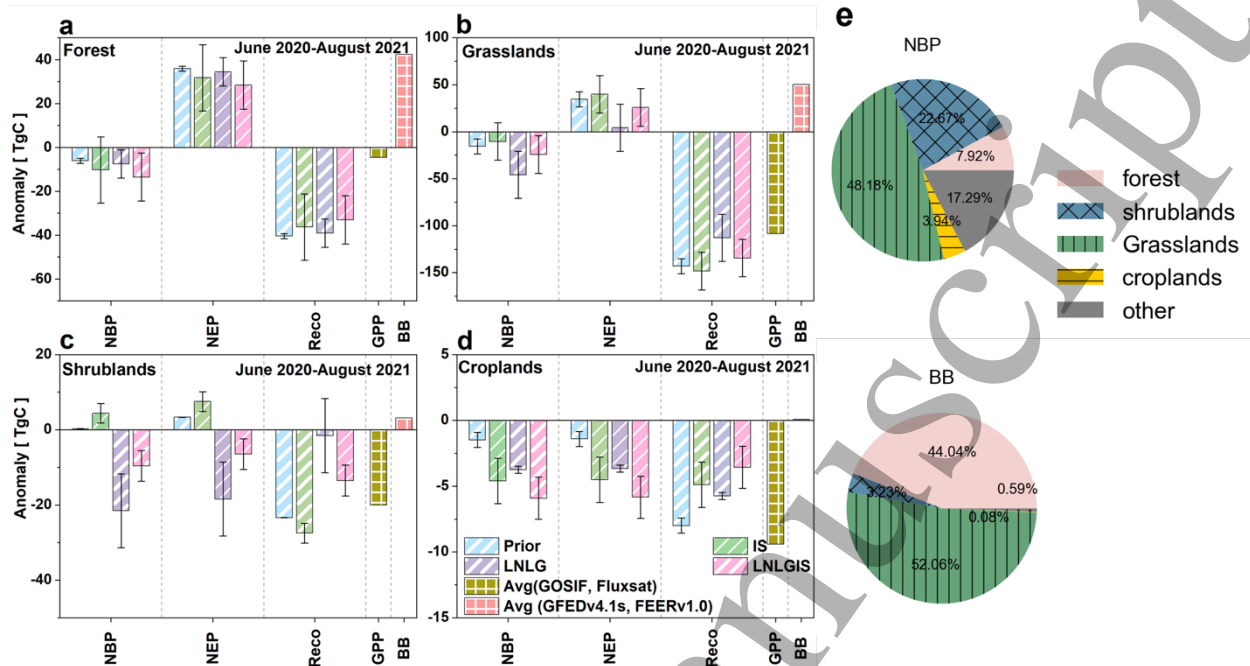


Figure 4. Anomalies of NBP and its constituent fluxes in SWNA during the June 2020 - August 2021 drought over different ecosystems. The study area was divided into different ecoregions based on the 2020 MODIS land cover data product (MOD12C1) and summarized into four types. The dominant ecosystem types include grasslands and shrublands (see Figure S9).

4. Discussion

4.1 Unexpected larger inhibition in Reco than in GPP during the 2020–2021 event

In the analyses, we noticed an unexpected larger inhibition in Reco than in GPP during the 2020–2021 event, which results in NEP increase. We noticed this phenomenon happened in both 2020 and 2021. We are aware that there existed uncertainties when deriving Reco from NBP, BB (fire emission) and GPP. To reduce such uncertainty, we employed two BB and GPP products. For NBP, a large array of datasets from both OCO-2 XCO₂ inversions and in-situ inversions were included. All results consistently pointed to such phenomenon, albeit of discrepancy in the anomaly magnitudes, making the finding reliable to some extent. We checked it by analyzing in-situ eddy flux measurements, and found this happened at some of these flux sites but not at most sites. During compound drought and fire events, there are evidence to support the occurrence of such phenomenon. The larger inhibition in Reco than in GPP could be explained by suppressed microbial soil respiration, which has also been found in previous studies in the post-drought and post-fire periods (Chen et al., 2019; Huang et al., 2021; Kopittke et al., 2014; Selsted et al., 2012). Further evidence, especially from intensive in-situ measurements, is critically needed to confirm this finding.

4.2 Discrepancy among the flux estimates by different inversion models

1
2
3 442 Although most inversion models have general agreement on the large carbon loss during the
4 443 event, the magnitude and even the direction of flux anomalies remain differ notably (See Table 2).
5 444 Firstly, satellite inversions estimate higher NBP anomalies than in-situ based inversions do. It
6 445 could be because that, the satellite inversion used vertical column CO₂ data instead of surface CO₂
7 446 data to infer carbon fluxes, in theory the column CO₂ data contain more signals than surface CO₂
8 447 did, especially the column CO₂ contain more CO₂ sources in the atmosphere, thus larger sink to
9 448 balance it in an inversion framework (mass balance between sink and source). Similarly, higher
10 449 estimates from satellite inversions than in-situ inversions were reported in previous studies about
11 450 the regional carbon sinks in Europe (Feng et al., 2016), US (Byrne et al., 2023) and China (He et
12 451 al., 2023b). Secondly, the difference in the regional carbon budget estimates among the three OCO-
13 452 2 MIP experiments and four in-situ based global inversions partly originate from this gap between
14 453 satellite inversions than in-situ inversions, as well as uncertainties among different inversion
15 454 frameworks (both due to inversion system design and assimilated data). To our knowledge, there
16 455 are quite few atmospheric CO₂ sites in and around SWNA, making the in-situ inversion less
17 456 reliable, especially in a global inversion framework. In addition, the SWNA is an arid region,
18 457 where vegetation signal is relative weak in a large proportion of the domain, making reliable
19 458 regional flux estimate challenging. In comparison, model ensemble could provide more reliable
20 459 estimates on regional flux and its anomaly, especially these constrained by satellite XCO₂
21 460 observations (He et al., 2023a; He et al., 2023b).

29 461 **4.3 Implications and future perspectives**

31 462 Our study provided a comprehensive assessment on the impact of the 2020–2021 drought
32 463 and associated wildfires in the SWNA on the terrestrial carbon budget using multiple datasets.
33 464 Such events are widespread over the globe in the context of climate warming, calling for more
34 465 research attention on this topic. We highlight that the impact of drought and post-drought (e.g.,
35 466 wildfires) should be considered together, as well as ecosystem recovery and resilience during the
36 467 whole period, which may offer new perspectives on how terrestrial ecosystems respond to climate
37 468 extremes. In addition, to better monitor the response of terrestrial ecosystems to drought and
38 469 following disturbance, we need to combine measurements from different scales, for example,
39 470 satellite observations, in-situ flux observation, atmospheric CO₂ concentration observations from
40 471 both in-situ and satellite platforms. Further efforts should also made to reduce uncertainties in fire
41 472 CO₂ emission estimates, especially encouraging to conduct it with top-down inversion frameworks
42 473 (van der Velde et al., 2021; Zheng et al., 2023).

48 474 **5. Conclusions**

50 475 In this study, we quantified the impact of the 2020–2021 drought in the SWNA on the terrestrial
51 476 carbon budget using the NBP estimates from atmospheric inversions of in-situ CO₂ and OCO-2
52 477 XCO₂ retrievals, two satellite-based GPP datasets, and two fire CO₂ emission datasets. We found
53 478 that the 2020–2021 drought and associated wildfires in SWNA led to a large CO₂ loss, an ensemble
54
55
56
57
58
59
60

1
2
3 479 mean of 95.07 TgC estimated by the satellite inversions using both nadir and glint XCO₂ retrievals
4
5 480 within the OCO-2 v10 MIP, greater than 80% of the annual total carbon sink. Furthermore, the
6
7 481 carbon loss in 2020 was primarily driven by fire emissions, whereas in 2021, it was predominantly
8
9 482 contributed by drought impacts on terrestrial carbon uptake. Additionally, satellite inversions
10
11 483 revealed that the substantial carbon loss was largely attributed to fire emissions from forests and
12
13 484 grasslands, coupled with reductions in carbon uptake resulting from drought impacts on grasslands
14
15 485 and shrublands. The atmospheric inversions using satellite or surface CO₂ observations reveal an
16
17 486 unexpected larger attenuation in Reco than in GPP over SWNA during the 2020–2021 event,
18
19 487 which largely compensates for its carbon release. Our study provides a new perspective on the
20
21 488 response of SWNA ecosystem carbon budget to the 2020–2021 drought and associated wildfires,
22
23 489 and an in-depth understanding of how it was impacted on a regional scale.
24

25 491 **Acknowledgments**

26
27 492 This research is funded by the National Natural Science Foundation of China (Grant No. 42277453
28
29 493 and 41907378). The OCO-2 XCO₂ data are produced by the Observing Carbon Observatory
30
31 494 project at the Jet Propulsion Laboratory, California Institute of Technology, and obtained from the
32
33 495 data archive at the NASA Goddard Earth Science Data and Information Services Center. We
34
35 496 acknowledge the Oak Ridge National Laboratory (ORNL) Distributed Active Archive Center
36
37 497 (DAAC) for providing the GFED4.1s dataset and NASA Goddard Space Flight Center for
38
39 498 providing the FEERv1.0 dataset. We also sincerely acknowledge the NOAA CarbonTracker team
40
41 499 and the NIES NISMON team for providing inverse flux estimates, which offer essential supports
42
43 500 to our study.

44 501 **Data Availability Statement**

45
46 502 The CAMS carbon flux data are publicly available at
47
48 503 [https://ads.atmosphere.copernicus.eu/cdsapp#!/dataset/cams-global-greenhouse-gas-inversion?](https://ads.atmosphere.copernicus.eu/cdsapp#!/dataset/cams-global-greenhouse-gas-inversion?tab=form)
49
50 504 [tab=form](https://ads.atmosphere.copernicus.eu/cdsapp#!/dataset/cams-global-greenhouse-gas-inversion?tab=form). The Jena CarboScope carbon flux data are publicly available at [http://www.bgc-](http://www.bgc-jena.mpg.de/CarboScope/)
51
52 505 [jena.mpg.de/CarboScope/](http://www.bgc-jena.mpg.de/CarboScope/). The CarbonTracker carbon flux data are publicly available at
53
54 506 <http://carbontracker.noaa.gov>. The NISMON-CO₂ carbon flux data are publicly available at
55
56 507 <https://www.nies.go.jp/doi/10.17595/20201127.001-e.html>. The GOSIF GPP dataset is publicly
57
58
59
60

1
2
3 available at <https://globalecology.unh.edu/data/GOSIF-GPP.html>. The GLEAM v3.6a root-zone
4
5 509 soil moisture is publicly available at <https://www.gleam.eu/#downloads>. The GLASS FAPAR
6
7 510 dataset is publicly available at <http://www.glass.umd.edu/Download.html>. The GFED4.1s is
8
9 511 publicly available at https://daac.ornl.gov/cgi-bin/dsviewer.pl?ds_id=1293. The FEERv1.0 dataset
10
11 512 is publicly available at <https://feer.gsfc.nasa.gov/data/emissions/>.

12 13 513 **References**

- 14
15 514 Ahlström, A., Raupach, M.R., Schurgers, G., Smith, B., Arneeth, A., Jung, M., Reichstein, M. et
16
17 515 al., 2015. The dominant role of semi-arid ecosystems in the trend and variability of the land
18
19 516 CO₂ sink. *Science*, 348: 895 - 899.
- 20 517 Baker, D.F., Bösch, H., Doney, S.C., O'Brien, D. and Schimel, D.S., 2010. Carbon source/sink
21
22 518 information provided by column CO₂ measurements from the Orbiting Carbon Observatory.
23
24 519 *Atmos. Chem. Phys.*, 10(9): 4145-4165.
- 25 520 Baker, D.F., Doney, S.C. and Schimel, D.S., 2006. Variational data assimilation for atmospheric
26
27 521 CO₂. *Tellus B: Chemical and Physical Meteorology*, 58(5): 359-365.
- 28 522 Basu, S., Baker, D.F., Chevallier, F., Patra, P.K., Liu, J. and Miller, J.B., 2018. The impact of
29
30 523 transport model differences on CO₂ surface flux estimates from OCO-2 retrievals of column
31
32 524 average CO₂. *Atmos. Chem. Phys.*, 18(10): 7189-7215.
- 33 525 Basu, S., Guerlet, S., Butz, A., Houweling, S., Hasekamp, O., Aben, I., Krummel, P. et al., 2013.
34
35 526 Global CO₂ fluxes estimated from GOSAT retrievals of total column CO₂. *Atmos. Chem.*
36
37 527 *Phys.*, 13(17): 8695-8717.
- 38 528 Beillouin, D., Schauburger, B., Bastos, A., Ciais, P. and Makowski, D., 2020. Impact of extreme
39
40 529 weather conditions on European crop production in 2018. *Philosophical Transactions of the*
41
42 530 *Royal Society B: Biological Sciences*, 375.
- 43 531 Bowman, K.W., Liu, J., Bloom, A.A., Parazoo, N.C., Lee, M., Jiang, Z., Menemenlis, D. et al.,
44
45 532 2017. Global and Brazilian Carbon Response to El Niño Modoki 2011–2010. *Earth and*
46
47 533 *Space Science*, 4: 637 - 660.
- 48 534 Byrne, B., Baker, D.F., Basu, S., Bertolacci, M., Bowman, K.W., Carroll, D., Chatterjee, A. et al.,
49
50 535 2023. National CO₂ budgets (2015–2020) inferred from atmospheric CO₂ observations in
51
52 536 support of the global stocktake. *Earth Syst. Sci. Data*, 15, 963–1004.
- 53 537 Chen, J., Zhang, Y., Luo, Y., Zhou, X., Jiang, Y., Zhao, J., Chen, Y. et al., 2019. Contrasting
54
55 538 responses after fires of the source components of soil respiration and ecosystem respiration.
56
57 539 *European Journal of Soil Science*, 70: 616 - 629.
- 58 540 Chen, Z., Huntzinger, D.N., Liu, J., Piao, S., Wang, X., Sitch, S., Friedlingstein, P. et al., 2021a.
59
60 541 Five years of variability in the global carbon cycle: comparing an estimate from the Orbiting
542
543 542 Carbon Observatory-2 and process-based models. *Environmental Research Letters*, 16(5):
054041.

- 1
2
3 544 Chen, Z., Liu, J., Henze, D.K., Huntzinger, D.N., Wells, K.C., Sitch, S., Friedlingstein, P. et al.,
4 545 2021b. Linking global terrestrial CO₂ fluxes and environmental drivers: inferences from the
5 546 Orbiting Carbon Observatory 2 satellite and terrestrial biospheric models. *Atmos. Chem.*
6 547 *Phys.*, 21(9): 6663-6680.
- 8 548 Chevallier, F., Fisher, M., Peylin, P., Serrar, S., Bousquet, P., Bréon, F.-M., Chédin, A. et al., 2005.
9 549 Inferring CO₂ sources and sinks from satellite observations: Method and application to
10 550 TOVS data. *Journal of Geophysical Research: Atmospheres*, 110(D24).
- 12 551 Chevallier, F., Remaud, M., O'Dell, C.W., Baker, D., Peylin, P. and Cozic, A., 2019a. Objective
13 552 evaluation of surface- and satellite-driven carbon dioxide atmospheric inversions. *Atmos.*
14 553 *Chem. Phys.*, 19(22): 14233-14251.
- 16 554 Chevallier, F., Remaud, M., O'Dell, C.W., Baker, D.J., Peylin, P. and Cozic, A., 2019b. Objective
17 555 evaluation of surface- and satellite-driven carbon dioxide atmospheric inversions.
18 556 *Atmospheric Chemistry and Physics*, 19: 14233-14251.
- 20 557 Ciais, P., Reichstein, M., Viovy, N., Granier, A., Ogée, J., Allard, V., Aubinet, M. et al., 2005.
21 558 Europe-wide reduction in primary productivity caused by the heat and drought in 2003.
22 559 *Nature*, 437(7058): 529-533.
- 24 560 Claverie, M., Matthews, J.L., Vermote, E.F. and Justice, C.O., 2016. A 30+ Year AVHRR LAI
25 561 and FAPAR Climate Data Record: Algorithm Description and Validation. *Remote. Sens.*, 8:
26 562 263.
- 28 563 Constenla-Villoslada, S., Liu, Y., Wen, J., Sun, Y. and Chonabayashi, S., 2022. Large-scale land
29 564 restoration improved drought resilience in Ethiopia's degraded watersheds. *Nature*
30 565 *Sustainability*, 5(6): 488-497.
- 32 566 Crowell, S., Baker, D., Schuh, A., Basu, S., Jacobson, A.R., Chevallier, F., Liu, J. et al., 2019. The
33 567 2015–2016 carbon cycle as seen from OCO-2 and the global in situ network. *Atmos. Chem.*
34 568 *Phys.*, 19(15): 9797-9831.
- 36 569 Dannenberg, M.P., Yan, D., Barnes, M.L., Smith, W.K., Johnston, M.R., Scott, R.L., Biederman,
37 570 J.A. et al., 2022. Exceptional heat and atmospheric dryness amplified losses of primary
38 571 production during the 2020 U.S. Southwest hot drought. *Global Change Biology*, 28: 4794
39 572 - 4806.
- 41 573 De Kauwe, M.G., Medlyn, B.E., Pitman, A.J., Drake, J.E., Ukkola, A.M., Griebel, A., Pendall, E.
42 574 et al., 2019. Examining the evidence for decoupling between photosynthesis and
43 575 transpiration during heat extremes. *Biogeosciences*, 16, 903–916.
- 45 576 Detmers, R.G., Hasekamp, O., Aben, I., Houweling, S., Van Leeuwen, T.T., Butz, A., Landgraf,
46 577 J. et al., 2015. Anomalous carbon uptake in Australia as seen by GOSAT. *Geophysical*
47 578 *Research Letters*, 42(19): 8177–8184.
- 49 579 Feldman, A. F., Zhang, Z., Yoshida, Y., Gentine, P., Chatterjee, A., Entekhabi, D., Joiner, J.,
50 580 & Poulter, B., 2023. A multi-satellite framework to rapidly evaluate extreme biosphere
51 581 cascades: The Western US 2021 drought and heatwave. *Global Change Biology*, 29, 3634–
52 582 3651.

- 1
2
3 583 Feng, L., Palmer, P.I., Parker, R.J., Deutscher, N.M., Feist, D.G., Kivi, R., Morino, I. et al., 2016.
4 584 Estimates of European uptake of CO₂ inferred from GOSAT XCO₂ retrievals: sensitivity to
5 585 measurement bias inside and outside Europe. *Atmospheric Chemistry and Physics*, 16: 1289-
6 586 1302.
- 7
8 587 Friedlingstein, P., O'Sullivan, M., Jones, M.W., Andrew, R.M., Gregor, L., Hauck, J., Le Quéré,
9 588 C. et al., 2022. Global Carbon Budget 2022. *Earth Syst. Sci. Data*, 14(11): 4811-4900.
- 10 589 Gatti, L.V., Gloor, M., Miller, J.B., Doughty, C.E., Malhi, Y.S., Domingues, L., Basso, L.S. et al.,
11 590 2014. Drought sensitivity of Amazonian carbon balance revealed by atmospheric
12 591 measurements. *Nature*, 506: 76-80.
- 13
14 592 Giglio, L., Randerson, J.T. and Werf, G.R., 2013. Analysis of daily, monthly, and annual burned
15 593 area using the fourth-generation global fire emissions database (GFED4). *Journal of*
16 594 *Geophysical Research: Biogeosciences*, 118: 317 - 328.
- 17
18 595 Green, J.K., Seneviratne, S.I., Berg, A.M., Findell, K.L., Hagemann, S., Lawrence, D.M. and
19 596 Gentine, P., 2019. Large influence of soil moisture on long-term terrestrial carbon uptake.
20 597 *Nature*, 565(7740): 476-479.
- 21
22 598 He, W., Jiang, F., Ju, W., Byrne, B., Xiao, J., Nguyen, N. T., et al. 2023a. Do state-of-the-art
23 599 atmospheric CO₂ inverse models capture drought impacts on the European land carbon
24 600 uptake? *Journal of Advances in Modeling Earth Systems*, 15, e2022MS003150.
- 25
26 601 He, W., Jiang, F., Ju, W., Chevallier, F., Baker, D. F., Wang, J., et al. 2023b. Improved constraints
27 602 on the recent terrestrial carbon sink over China by assimilating OCO-2 XCO₂ retrievals.
28 603 *Journal of Geophysical Research: Atmospheres*, 128, e2022JD037773.
- 29
30 604 Hersbach, H., Bell, B., Berrisford, P., Hirahara, S., Horányi, A., Muñoz-Sabater, J., Nicolas, J. et
31 605 al., 2020. The ERA5 global reanalysis. *Quarterly Journal of the Royal Meteorological*
32 606 *Society*, 146: 1999 - 2049.
- 33
34 607 Houghton, J.T., 2014. *Climate Change 2013 - The Physical Science Basis: Working Group I*
35 608 *Contribution to the Fifth Assessment Report of the Intergovernmental Panel on Climate*
36 609 *Change*.
- 37
38 610 Huang, H., Calabrese, S. and Rodríguez-Iturbe, I., 2021. Variability of ecosystem carbon source
39 611 from microbial respiration is controlled by rainfall dynamics. *Proceedings of the National*
40 612 *Academy of Sciences*, 118.
- 41
42 613 Ichoku, C. and Ellison, L.T., 2013. Global top-down smoke aerosol emissions estimation using
43 614 satellite fire radiative power measurements. *Atmospheric Chemistry and Physics*, 14: 6643-
44 615 6667.
- 45
46 616 Iida, Y., Takatani, Y., Kojima, A. and Ishii, M., 2021. Global trends of ocean CO₂ sink and ocean
47 617 acidification: an observation-based reconstruction of surface ocean inorganic carbon
48 618 variables. *Journal of Oceanography*, 77: 323-358.
- 49
50 619 Ito, A. and Inatomi, M., 2012. Use of a process-based model for assessing the methane budgets of
51 620 global terrestrial ecosystems and evaluation of uncertainty. *Biogeosciences*, 9(2): 759-773.
- 52
53 621 Jacobson, A. R., Schuldt, K. N., Tans, P., Andrews, A., Miller, J. B., Oda, T., Basu, S., et al., 2023.
54 622 *CarbonTracker CT2022*.
- 55
56
57
58
59
60

- 1
2
3 623 Jacobson, A. R., Schuldt, K. N., Tans, P., Andrews, A., Miller, J. B., Oda, T., Basu, S., et al., 2023.
4 624 CarbonTracker CT-NRT.v2023-4.
- 5
6 625 Jiang, F., Wang, H., Chen, J. M., Ju, W., Tian, X., Feng, S., et al. 2021. Regional CO₂ fluxes from
7 626 2010 to 2015 inferred from GOSAT XCO₂ retrievals using a new version of the Global
8 627 Carbon Assimilation System. *Atmospheric Chemistry and Physics*, 21(3), 1963-1985.
- 9
10 628 Joiner, J., & Yoshida, Y., 2020. Satellite-based reflectances capture large fraction of variability in
11 629 global gross primary production (GPP) at weekly time scales. *Agricultural and Forest
12 630 Meteorology*, 291, 108092.
- 13
14 631 Jones, M.W., Andrew, R.M., Peters, G.P., Janssens-Maenhout, G., De-Gol, A.J., Ciais, P., Patra,
15 632 P.K. et al., 2021. Gridded fossil CO₂ emissions and related O₂ combustion consistent with
16 633 national inventories 1959–2018. *Scientific Data*, 8(1): 2.
- 17
18 634 Kiel, M., O'Dell, C.W., Fisher, B., Eldering, A., Nassar, R., MacDonald, C.G. and Wennberg,
19 635 P.O., 2019. How bias correction goes wrong: measurement of XCO₂ affected by erroneous
20 636 surface pressure estimates. *Atmos. Meas. Tech.*, 12(4): 2241-2259.
- 21
22 637 Kopittke, G.R., Tietema, A., Loon, E.E.v. and Asscheman, D., 2014. Fourteen Annually Repeated
23 638 Droughts Suppressed Autotrophic Soil Respiration and Resulted in an Ecosystem Change.
24 639 *Ecosystems*, 17: 242-257.
- 25
26 640 Krol, M., Houweling, S., Bregman, B., Van den Broek, M., Segers, A., Van Velthoven, P., Peters,
27 641 W. et al., 2005. The two-way nested global chemistry-transport zoom model TM5: algorithm
28 642 and applications. *Atmospheric Chemistry and Physics*, 5(2): 417-432.
- 29
30 643 Kwon, M. J., Ballantyne, A., Ciais, P., Bastos, A., Chevallier, F., Liu, Z., et al., 2021. Siberian
31 644 2020 heatwave increased spring CO₂ uptake but not annual CO₂ uptake. *Environmental
32 645 Research Letters*, 16(12), 124030.
- 33
34 646 Li, X. and Xiao, J., 2019. A Global, 0.05-Degree Product of Solar-Induced Chlorophyll
35 647 Fluorescence Derived from OCO-2, MODIS, and Reanalysis Data. *Remote. Sens.*, 11: 517.
- 36
37 648 Li, X., Ryu, Y., Xiao, J., Dechant, B., Liu, J., Li, B., et al., 2023. New-generation geostationary
38 649 satellite reveals widespread midday depression in dryland photosynthesis during 2020
39 650 western U.S. heatwave. *Science Advances*, 9(31), eadi0775.
- 40
41 651 Liu, J., Baskaran, L., Bowman, K., Schimel, D., Bloom, A.A., Parazoo, N.C., Oda, T. et al., 2021.
42 652 Carbon Monitoring System Flux Net Biosphere Exchange 2020 (CMS-Flux NBE 2020).
43 653 *Earth Syst. Sci. Data*, 13(2): 299-330.
- 44
45 654 Liu, J., Bowman, K.W., Schimel, D.S., Parazoo, N.C., Jiang, Z., Lee, M., Bloom, A.A. et al., 2017.
46 655 Contrasting carbon cycle responses of the tropical continents to the 2015–2016 El Niño.
47 656 *Science*, 358.
- 48
49 657 Liu, Z., Zeng, N., Liu, Y., Kalnay, E., Asrar, G., Wu, B., Cai, Q. et al., 2022. Improving the joint
50 658 estimation of CO₂ and surface carbon fluxes using a constrained ensemble Kalman filter in
51 659 COLA (v1.0). *Geosci. Model Dev.*, 15(14): 5511-5528.
- 52
53 660 Luo, L., Apps, D., Arcand, S., Xu, H., Pan, M. and Hoerling, M.P., 2017. Contribution of
54 661 temperature and precipitation anomalies to the California drought during 2012–2015.
55 662 *Geophysical Research Letters*, 44: 3184 - 3192.
- 56
57
58
59
60

- 1
2
3 663 Martens, B., Miralles, D.G., Lievens, H., Schalie, R.v.d., Jeu, R.d., Fernández-Prieto, D., Beck,
4 664 H.E. et al., 2016. GLEAM v3: satellite-based land evaporation and root-zone soil moisture.
5 665 Geoscientific Model Development, 10: 1903-1925.
6 666 Martens, B., Miralles, D.G., Lievens, H., Van Der Schalie, R., De Jeu, R.A., Fernández-Prieto, D.,
7 667 Beck, H.E. et al., 2017. GLEAM v3: Satellite-based land evaporation and root-zone soil
8 668 moisture. Geoscientific Model Development, 10(5): 1903-1925.
9 669 Masarie, K., Peters, W., Jacobson, A. and Tans, P., 2014. ObsPack: a framework for the
10 670 preparation, delivery, and attribution of atmospheric greenhouse gas measurements. Earth
11 671 System Science Data, 6(2): 375-384.
12 672 Meehl, G.A. and Tebaldi, C., 2004. More Intense, More Frequent, and Longer Lasting Heat Waves
13 673 in the 21st Century. Science, 305: 994 - 997.
14 674 Miller, S.M., Saibaba, A.K., Trudeau, M.E., Mountain, M.E. and Andrews, A.E., 2020.
15 675 Geostatistical inverse modeling with very large datasets: an example from the Orbiting
16 676 Carbon Observatory 2 (OCO-2) satellite. Geosci. Model Dev., 13(3): 1771-1785.
17 677 Niwa, Y., Ishijima, K., Ito, A. and Iida, Y., 2022. Toward a long-term atmospheric CO₂ inversion
18 678 for elucidating natural carbon fluxes: technical notes of NISMON-CO₂ v2021.1. Progress
19 679 in Earth and Planetary Science, 9(1): 42.
20 680 Peiro, H., Crowell, S., Schuh, A., Baker, D.F., O'Dell, C., Jacobson, A.R., Chevallier, F. et al.,
21 681 2022. Four years of global carbon cycle observed from the Orbiting Carbon Observatory 2
22 682 (OCO-2) version 9 and in situ data and comparison to OCO-2 version 7. Atmos. Chem.
23 683 Phys., 22(2): 1097-1130.
24 684 Peters, W., Jacobson, A.R., Sweeney, C., Andrews, A.E., Conway, T.J., Masarie, K., Miller, J.B.
25 685 et al., 2007. An atmospheric perspective on North American carbon dioxide exchange:
26 686 CarbonTracker. Proceedings of the National Academy of Sciences, 104(48): 18925-18930.
27 687 Peters, W., Miller, J., Whitaker, J., Denning, A., Hirsch, A., Krol, M., Zupanski, D. et al., 2005.
28 688 An ensemble data assimilation system to estimate CO₂ surface fluxes from atmospheric trace
29 689 gas observations. Journal of Geophysical Research: Atmospheres, 110(D24).
30 690 Philip, S., Johnson, M.S., Baker, D.F., Basu, S., Tiwari, Y.K., Indira, N.K., Ramonet, M. et al.,
31 691 2022. OCO-2 Satellite-Imposed Constraints on Terrestrial Biospheric CO₂ Fluxes Over
32 692 South Asia. Journal of Geophysical Research: Atmospheres, 127(3): e2021JD035035.
33 693 Philip, S., Johnson, M.S., Potter, C., Genovesse, V., Baker, D.F., Haynes, K.D., Henze, D.K. et
34 694 al., 2019. Prior biosphere model impact on global terrestrial CO₂ fluxes estimated from
35 695 OCO-2 retrievals. Atmos. Chem. Phys., 19(20): 13267-13287.
36 696 Qiu, B., Ge, J., Guo, W., Pitman, A.J. and Mu, M., 2020. Responses of Australian Dryland
37 697 Vegetation to the 2019 Heat Wave at a Subdaily Scale. Geophysical Research Letters, 47.
38 698 Rödenbeck, C., Houweling, S., Gloor, M. and Heimann, M., 2003. CO₂ flux history 1982–2001
39 699 inferred from atmospheric data using a global inversion of atmospheric transport.
40 700 Atmospheric Chemistry and Physics, 3: 1919-1964.
41 701 Schuldt KN, Mund J, Luijkx IT, Aalto T, Abshire JB, Aikin K, Andrews A, Aoki S, Apadula F,
42 702 Baier B, Bakwin P, Bartyzel J, Bentz G, Bergamaschi P, Beyersdorf A, Biermann T, Biraud

1
2
3
4
5
6
7
8
9
10
11
12
13
14
15
16
17
18
19
20
21
22
23
24
25
26
27
28
29
30
31
32
33
34
35
36
37
38
39
40
41
42
43
44
45
46
47
48
49
50
51
52
53
54
55
56
57
58
59
60

703 SC, Boenisch H, Bowling D, Brailsford G, Chen G, Chen H, Chmura L, Clark S, Climadat
704 S, Colomb A, Commane R, Conil S, Cox A, Cristofanelli P et al.,2021a. Multi-laboratory
705 compilation of atmospheric carbon dioxide data for the period 1957–2019;
706 obspack_co2_1_GLOBALVIEWplus_v6.1_2021a-03-01. NOAA Global Monitoring
707 Laboratory.

708 Schuldt KN, Jacobson AR, Aalto T, Andrews A, Bakwin P, Bergamaschi P, Biermann T, Biraud
709 SC, Chen H, Colomb A, Conil S, Cristofanelli P, De Mazière M, De Wekker S, Delmotte
710 M, Dlugokencky E, Emmenegger L, Fischer ML, Hatakka J, Heliasz M, Hermanssen O,
711 Holst J, Jaffe D, Karion A, Kazan V, Keronen P, Kominkova K, Kubistin D, Laurent O,
712 Laurila T, et al.,2021b. Multi-laboratory compilation of atmospheric carbon dioxide data for
713 the period 2020–2021b; obspack_co2_1_NRT_v6.1.1_2021b-05-17. NOAA Earth System
714 Research Laboratory, Global Monitoring Laboratory.

715 Schuldt KN, Aalto, T., Andrews, A., Aoki, S., Apadula, F., Arduini, J., Baier, B., et al., 2022.
716 Multi-laboratory compilation of atmospheric methane data for the period 1983-2021;
717 obspack_ch4_1_GLOBALVIEWplus_v5.0_2022-10-17; NOAA Earth System Research
718 Laboratory, Global Monitoring Laboratory.

719 Selsted, M.B., van der Linden, L., Ibrom, A., Michelsen, A., Larsen, K.S., Pedersen, J.K.,
720 Mikkelsen, T.N. et al., 2012. Soil respiration is stimulated by elevated CO₂ and reduced by
721 summer drought: three years of measurements in a multifactor ecosystem manipulation
722 experiment in a temperate heathland (CLIMAITE). *Global Change Biology*, 18(4): 1216-
723 1230.

724 Smith, N.E., Kooijmans, L.M.J., Koren, G., van Schaik, E., van der Woude, A.M., Wanders, N.,
725 Ramonet, M. et al., 2020. Spring enhancement and summer reduction in carbon uptake
726 during the 2018 drought in northwestern Europe. *Philosophical Transactions of the Royal
727 Society B: Biological Sciences*, 375.

728 Sun, Y., Frankenberg, C., Wood, J.D., Schimel, D.S., Jung, M., Guanter, L., Drewry, D.T. et al.,
729 2017. OCO-2 advances photosynthesis observation from space via solar-induced chlorophyll
730 fluorescence. *Science*, 358.

731 Tomita, H. and Satoh, M., 2004. A new dynamical framework of nonhydrostatic global model
732 using the icosahedral grid. *Fluid Dynamics Research*, 34(6): 357.

733 Van Der Werf, G.R., Randerson, J.T., Giglio, L., Van Leeuwen, T.T., Chen, Y., Rogers, B.M.,
734 Mu, M. et al., 2017. Global fire emissions estimates during 1997–2016. *Earth System
735 Science Data*, 9(2): 697-720.

736 van der Velde, I.R., van der Werf, G.R., Houweling, S. et al., 2021. Vast CO₂ release from
737 Australian fires in 2019–2020 constrained by satellite. *Nature*, 597, 366–369.

738 Vicente-Serrano, S. M., Beguería, S., & López-Moreno, J. I., 2010. A multiscalar drought index
739 sensitive to global warming: The standardized precipitation evapotranspiration index.
740 *Journal of Climate*, 23, 1696–1718.

741 Wees, D.v., Werf, G.v.d., Randerson, J.T., Rogers, B.M., Chen, Y., Veraverbeke, S., Giglio, L. et
742 al., 2022. Global biomass burning fuel consumption and emissions at 500-m spatial

- 1
2
3 743 resolution based on the Global Fire Emissions Database (GFED). *Geosci. Model Dev.*, 15,
4 744 8411–8437.
- 5
6 745 Williams, A.P., Cook, B.I. and Smerdon, J.E., 2022. Rapid intensification of the emerging
7 746 southwestern North American megadrought in 2020–2021. *Nature Climate Change*, 12: 232
8 747 - 234.
- 9
10 748 Wolf, S., Keenan, T.F., Fisher, J.B., Baldocchi, D.D., Desai, A.R., Richardson, A.D., Scott, R.L.
11 749 et al., 2016. Warm spring reduced carbon cycle impact of the 2012 US summer drought.
12 750 *Proceedings of the National Academy of Sciences*, 113: 5880 - 5885.
- 13
14 751 Xiao, Z., Liang, S., Sun, R., Wang, J. and Jiang, B., 2015. Estimating the fraction of absorbed
15 752 photosynthetically active radiation from the MODIS data based GLASS leaf area index
16 753 product. *Remote Sensing of Environment*, 171: 105-117.
- 17
18 754 Zacharias, S., Koppe, C. and Mücke, H.G., 2014. Climate Change Effects on Heat Waves and
19 755 Future Heat Wave-Associated IHD Mortality in Germany. *Climate*, 3: 100-117.
- 20
21 756 Zeng, N., Mariotti, A. and Wetzel, P.J., 2005. Terrestrial mechanisms of interannual CO₂
22 757 variability. *Global Biogeochemical Cycles*, 19.
- 23
24 758 Zhao, H., Jia, G., Xu, X. and Zhang, A., 2022. Contrasting responses of vegetation production to
25 759 rainfall anomalies across the Northeast China Transect. *Journal of Geophysical Research:*
26 760 *Biogeosciences*, 127(6): e2022JG006842.
- 27
28 761 Zhao, M. and Running, S.W., 2010. Drought-Induced Reduction in Global Terrestrial Net Primary
29 762 Production from 2000 Through 2009, *Science*, 329(5994):940-3.
- 30
31 763 Zhang, Y., Fang, J., Smith, W. K., Wang, X., Gentine, P., Scott, R.
32 764 L., Migliavacca, M., Jeong, S., Litvak, M., & Zhou, S., 2023. Satellite solar-induced
33 765 chlorophyll fluorescence tracks physiological drought stress development during 2020
34 766 southwest US drought. *Global Change Biology*, 29, 3395–3408.
- 35
36 767 Zheng, B., Ciais, P., Chevallier, F., Yang, H., Canadell, J. G., Chen, Y., et al., 2023. Record-high
37 768 CO₂ emissions from boreal fires in 2021. *Science*, 379(6635), 912-917.
- 38
39
40
41
42
43
44
45
46
47
48
49
50
51
52
53
54
55
56
57
58
59
60